MDPI

Article

Design of a High Efficiency High Step-Up/Step-Down Bidirectional Isolated DC–DC Converter

Yu-En Wu *[ID] and **Pin-Jyun Lin**

Department of Electronic Engineering, National Kaohsiung University of Science and Technology, Kaohsiung 824, Taiwan; F108112122@nkust.edu.tw
* Correspondence: yew@nkust.edu.tw; Tel.: +886-7-6011000 (ext. 32511)

Abstract: This paper presents a novel bidirectional DC–DC converter, equipped with a three-winding coupled inductor, that can be applied to high-voltage, bidirectional DC–DC energy conversion and meet battery charging and discharging requirements. The architecture consists of a semi-Z-source converter and a forward–flyback converter featuring a three-winding coupled inductor with an iron core. This proposed topology retains the current continuity characteristics of the low-voltage side, all switches possess the zero-voltage switching feature, and the switches on the low-voltage side in the step-down mode have a synchronous rectification function. A 500-W bidirectional converter is implemented to examine the practicality and feasibility of the proposed topology. The relatively streamlined design of the converter can greatly reduce production costs. In the step-up and step-down modes, the maximum energy conversion efficiencies are 95.74% and 96.13%, respectively.

Keywords: bidirectional DC–DC converter; synchronous rectification; three-winding coupled inductor; zero voltage switching

1. Introduction

Since the Industrial Revolution, fossil fuels have been used extensively. The environment has been substantially altered on a global scale through the greenhouse effect, as indicated by global warming, increases in the emission of particulate matter smaller than 2.5 µm, and other phenomena. Thus, environmental issues have received growing attention in recent years. Relevant efforts include using renewable energy sources such as solar power, wind power, and hydropower as alternatives to petroleum [1]. Natural hazards can hinder the reliable generation of power from renewable energy sources. Energy storage systems generally seek to ensure the stability of power output. When a surplus of energy is available, the excess energy can be placed in the energy storage system and released when necessary [2].

Figure 1 presents a block diagram of a renewable energy supply system. Power is provided to the microgrid through this system and the energy storage system to maintain a stable power supply [3,4].

With rapid advances in systems for power generation from renewable energy sources, in order to reduce the cost and volume, in recent years, many bidirectional converters with step-up/step-down function have presented. The bidirectional direct current (DC)–DC converter has also been widely employed in various industrial applications, including hybrid vehicles [5], auxiliary power supplies, and battery charging–discharging for uninterruptible power systems (UPS). Moreover, vehicles have become indispensable tools for transportation in modern life. In view of the increasing attention paid to plug-in hybrid electric vehicles (PHEVs) [6], the advantages of which include low pollution and low energy consumption, a bidirectional DC–DC converter with a three-winding coupled inductor is presented in this paper, as shown in Figure 2. This converter can be applied to PHEVs' energy storage systems as well as to renewable energy supply systems. Excess energy is

kept in the energy storage system for use when the system is under peak load. Specifically, at such times, the stored energy is supplied to the grid for voltage stabilization.
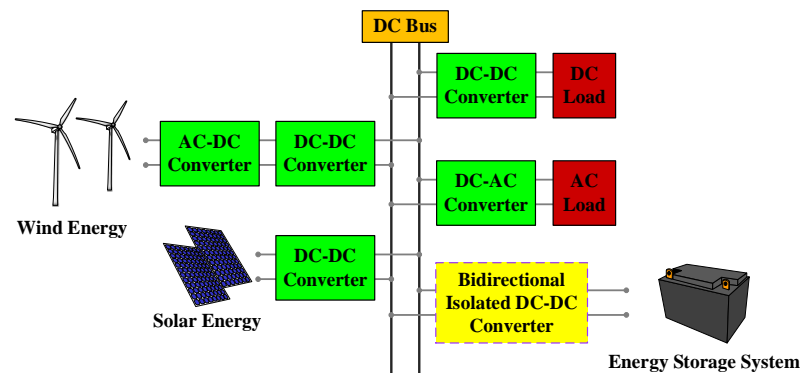

Figure 1. Configuration of the diversified energy system of the energy storage system.
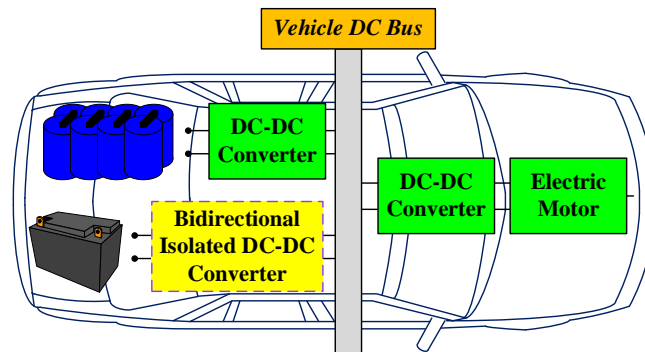

Figure 2. Hybrid energy source of a PHEV.

Conventional non-isolated converters include boost converters, buck converters, and single-ended primary-inductor converters. Conventional isolated converters include flyback converters, forward converters, and push–pull converters. Isolated converters are more widely used because they better ensure safety [7–9], provide galvanic isolation, and improve noise immunity. The conventional boost converter has a simple structure and is low in cost. It can easily increase the output voltage and is suitable for use in conditions involving low voltage gain. Such converters are typically employed in power factor correction circuits [10–12] and on the primary side of maximum power point tracking in photovoltaic power generation systems [13–15]. In [16–18], such converters are mainly used in electric vehicles, light-emitting diodes (LEDs), and high-intensity discharge lamps. They are also applied to the low–high conversion of DC voltages (e.g., 48 to 380 V) in computer and communications applications. The advantages of such converters include the activation of the power switch, the small number of parts, and the low cost. They are typically used in isolated power supplies, chargers for mobile devices, and medium and low output power applications [19].

In [20], a high conversion ratio is achieved by using a capacitor charged in parallel and discharged in series with a coupled inductor [21]. Although the main switches in this converter are operated under zero voltage switching (ZVS), which increases system efficiency, the auxiliary switch still performs hard switching, and the voltage diversity of the converter is extremely limited. Hard switching of the converter limits the switching frequency, and the inclusion of a coupled inductor complicates the design. In [22], gallium nitride (GAN) switches are applied to the same topology, which is operated at 1 MHz, to greatly reduce circuit size and increase energy conversion efficiency. However, such circuits are expensive; moreover, the high-frequency switching results in an excessively high switching loss. Although a ZVS feature is present under a 30% load, when the converter is

operated under the full load, the hard switch feature of the power switches causes a large switching loss.

The non-isolated bidirectional DC–DC converters in [23–27] have neither a common ground nor an isolation ground between the low- and high-voltage sides, reducing safety and industrial applicability. In [28], two inductors are used on the low-voltage side to reduce the high current flow through the inductors and switches. However, many magnetic components cause circuit volume and cost increase and high copper wire loss. In [29], the topology is developed by integrating a three-winding coupled inductor, three switched capacitors, and a flyback converter. Specifically, the topology comprises a set of interleaved flyback converters on the low-voltage side and, on the high-voltage side, two converters similar to half-bridge converters. It can be used to limit cross-leakage in energy recovery and improve energy conversion efficiency. The shortcomings of this topology are the relatively complex circuit operation and the required addition of an energy recovery circuit. Moreover, the basis of this topology, the flyback converter increases ripple currents [30]. In [31], an isolated bidirectional DC–DC converter with two integrated non-dissipative inductor–capacitor–diode (LCD) snubbers is presented. This topology combines the inductance circuit in energy recovery [32–34] with a transformer to enhance power density. The topology improves the energy recovery of leakage inductance on conventional flyback converters. Moreover, the bidirectional power flow increases the practicality of this topology [35–38]. Although it is simple to control, the input current is discontinuous, and the inclusion of the recovery circuit adds to the overall circuit complexity. In addition, because the power must flow through two series of diodes to the output port in the conduction mode, power consumption is doubled and the energy conversion efficiency is compromised.

In addition to two-port bidirectional converters, many three-port bidirectional converters have also been proposed in recent years [39–41], which have a wider range of applications. In [39], the bidirectional converter achieves high step-up and high step-down but it only provides 250 W. In [40], the topology only uses two switches that greatly reduce the cost of converter. However, power is too small to PV system. Furthermore, it only provides unidirectional energy transmission. In [41], the snubber replaces extra active switches but the converter still has five switches.

In order to improve the above shortcomings, this paper proposes a high efficiency and high step-up/step-down isolated bidirectional DC/DC converter, which has the following advantages: (1) it has high energy conversion efficiency, (2) it is safe to use and has relatively low circuit costs, (3) all power switches can achieve ZVS, (4) an inductance circuit is employed to facilitate energy recovery, and (5) the low-voltage side has the synchronous rectification function in step-down mode.

2. Circuit Architecture and Operational Principles

The proposed isolated bidirectional DC–DC converter is shown in Figure 3. The components are defined as follows. V_L and V_H are the low-side and high-side power ports, respectively. The four switches are designated as S_1–S_4. D_{S1}–D_{S4} and C_{S1}–C_{S4} represent the body diodes and parasitic capacitances of the switches, respectively. The other components are three capacitators, designated as C_1–C_3, and a three-winding coupled inductor. The coupled inductor is composed of leakage inductances L_{lk1}, L_{lk2}, and L_{lk3}; magnetizing inductance L_{m1}; and turns ratio N. The operational principles of the proposed converter in the step-up and step-down modes are analyzed. The corresponding components, voltage polarity, and current direction of the converter are presented in Figure 3. All magnetic components are operated in CCM. To simplify the analysis of the operational principle, several assumptions are made as follows:

(1) Switches and their parasitic diodes are ideal and the parasitic capacitance is considered.
(2) The capacitance values C1, C2, and C3 are infinite.
(3) The leakage inductance values L_{lk1} and L_{lk2} are substantially much lower than the magnetizing inductance Lm1.

(4) N1 is equal to N2 but less than N3, and the ratios of N1/N3 and N2/N3 are defined as N.

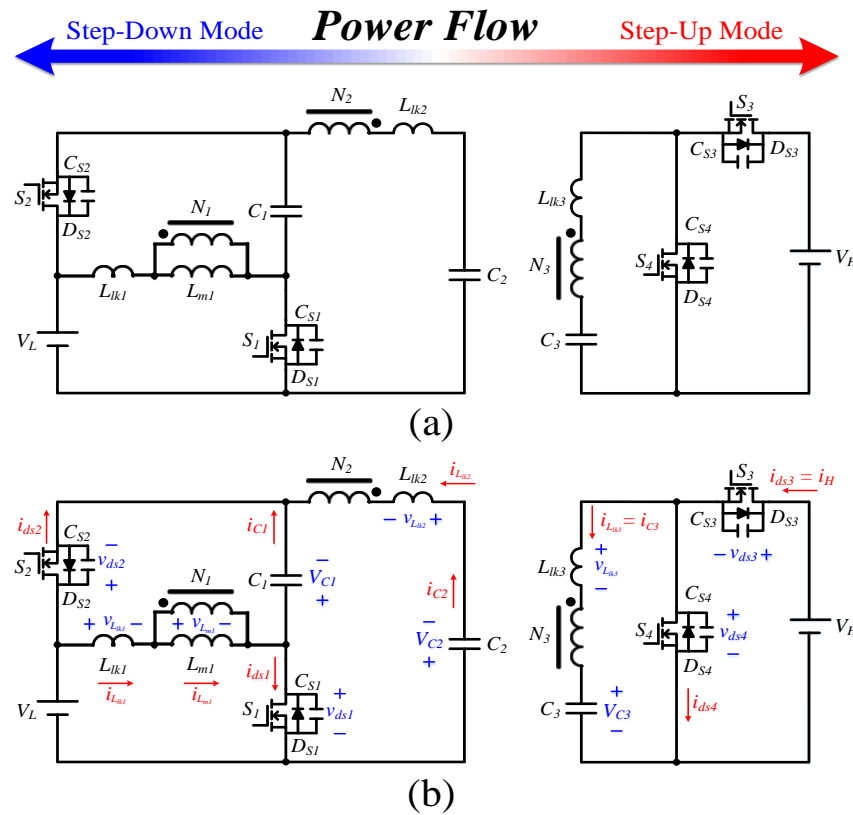**Figure 3.** The proposed topology: (**a**) diagram of the bidirectional isolated DC–DC converter and (**b**) the definitions for the equivalent circuit diagram.

A. Step-Up Mode

　　In the step-up mode, the signals of switches S1 and S2 are V_{gs1} and V_{gs2}, respectively. Moreover, V_{gs3} and V_{gs4}, the signals of switches S3 and S4, are in the OFF state. The key waveforms in the step-up mode are shown in Figure 4. An operating cycle can be divided into five modes, as shown in Figure 5a–e.

Mode 1 (t_0–t_1)

　　At the beginning of this mode, when time $t = t_0$, all switch signals are in the OFF state. The leakage inductance L_{lk2} extracts the energy from the parasitic capacitance CS1 of switch S1 to achieve ZVS, and the parasitic capacitance CS2 of switch S2 stores energy until S2 is turned OFF. The energy stored in L_{lk3} is recycled to C3 through D_{S4}. When the current L_{lk3} drops to zero, the mode ends. The equivalent circuit diagram of mode 1 is presented in Figure 5a.

Mode 2 (t_1–t_2)

　　At the beginning of this mode, when $t = t_1$, switch S1 is turned ON and switch S2 is turned OFF, so switch signals V_{gs1} and V_{gs2} are in the ON and OFF states, respectively. The low-voltage side V_L supplies energy to the magnetizing inductance L_{m1}. The energy stored in leakage inductance L_{lk1} is transmitted to the high-voltage side VH and capacitor C3 via the coupled inductor and the body diode D_{S3} of switch S3. When the capacitors C1 and C2 resonate with the leakage inductance L_{lK2}, mode 2 ends as switch S1 is turned OFF. The equivalent circuit diagram of mode 2 is presented in Figure 5b.

Mode 3 (t_2–t_3)

　　At the beginning of this mode, when time $t = t_2$, all switch signals are in the OFF state. The leakage inductance L_{lk1} extracts the energy from the parasitic capacitance C_{S2} of switch S2 to achieve ZVS. The parasitic capacitance C_{S1} of switch S1 stores energy until

S1 is turned OFF. On the high-voltage side, the energy stored in L_{lk3} and capacitor C3 are released to V_H through D_{S3}. When the current of i_{Llk3} is zero, mode 3 ends. The equivalent circuit diagram of this mode is presented in Figure 5c.

Mode 4 (t–t_4)

In mode 4, which begins when $t = t_3$, the switch signal V_{gs2} is in the ON state, whereas the switch signal V_{gs1} is in the OFF state. Magnetizing inductance L_{m1} and capacitor C2 release energy to capacitor C3 through the coupled inductor and through body diode D_{S4} of switch S4. The leakage inductance Llk1 releases energy to capacitor C1 through switch S2 until the current voltage in S2 is zero, at which point mode 4 ends. The equivalent circuit diagram of this mode is presented in Figure 5d.

Mode 5 (t_4–t_5)

In this mode, which starts when $t = t_4$, the switch signals are the same as those in the previous mode in this time interval. The energy of L_{lK1} decreases gradually, and the leakage inductance L_{lK2} releases energy through switch S2. On the high-voltage side, the previous operating mode is maintained. When switch S2 is turned OFF, this mode ends. Its equivalent circuit diagram is presented in Figure 5e.
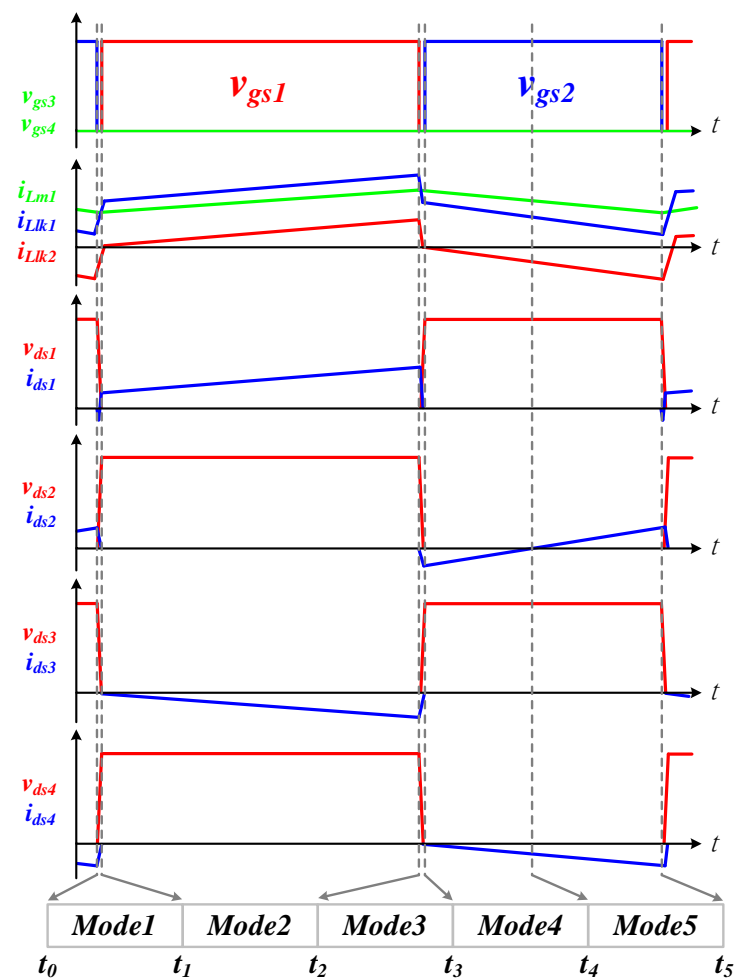

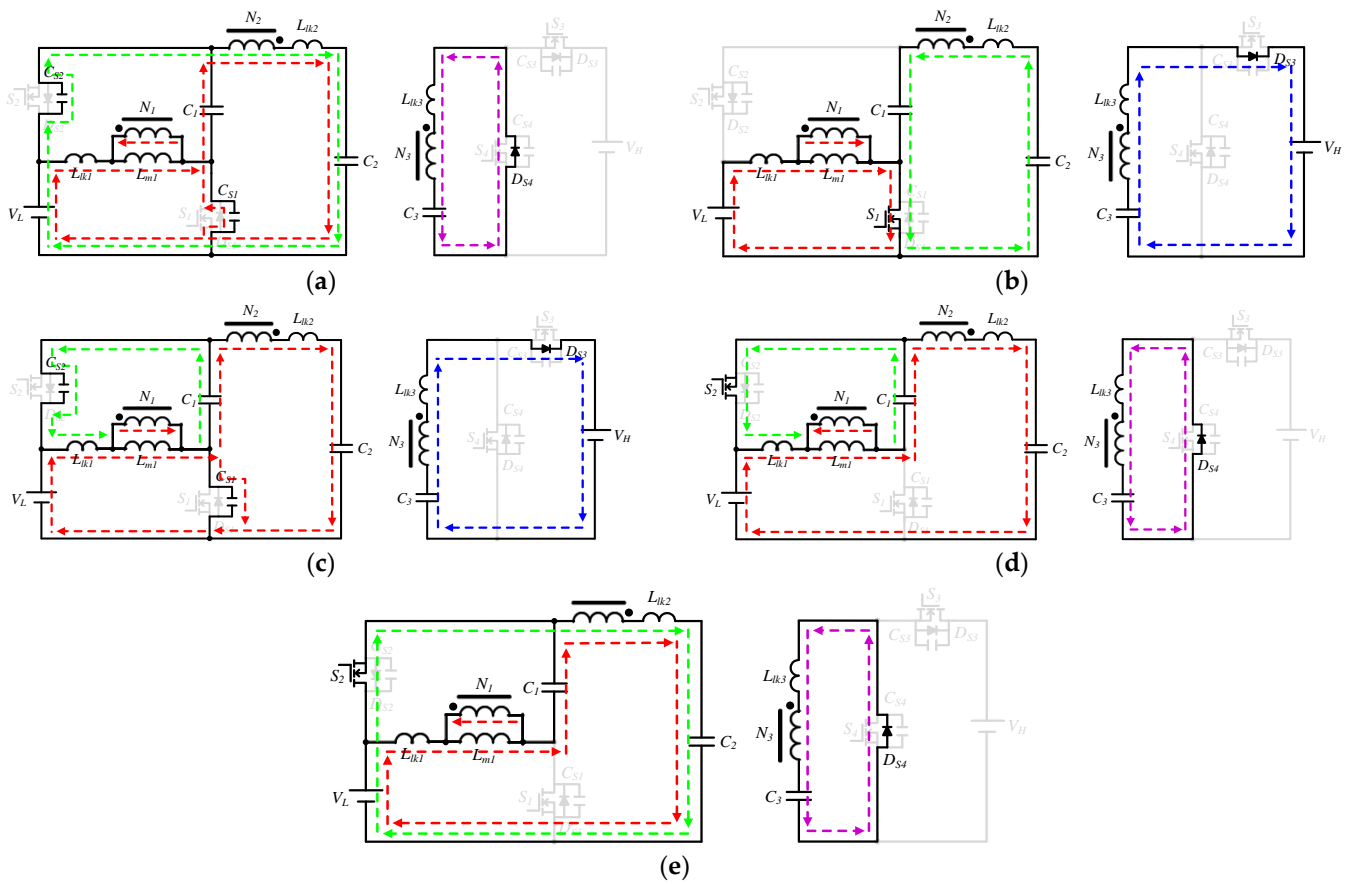**Figure 4.** Key waveforms of the proposed topology in the step-up mode.

Figure 5. Equivalent circuit diagram of (**a**) mode 1, (**b**) mode 2, (**c**) mode 3, (**d**) mode 4, and (**e**) mode 5 in the step-up mode.

B. Step-Down Mode

In the step-down mode, the operating signal is a complementary signal comprising two sets of signals: V_{gs1}–V_{gs3} and V_{gs2}–V_{gs4}. The key waveforms of the proposed topology in the step-down mode are shown in Figure 6. An operating cycle is divided into seven operating modes, as shown in Figure 7a–g.

Mode 1 (t_0–t_1)

This mode begins when $t = t_0$. All switch signals are in the OFF state. The leakage inductance L_{lk3} draws from the electric charges from parasitic capacitor C_{S3} of switch S3 to achieve ZVS. Moreover, the leakage inductance L_{lk3} charges the parasitic capacitance CS4 of switch S4 until S4 is turned OFF. Capacitor C2 transfers energy to capacitor C1 and leakage inductance L_{lk2}. The energy of the magnetizing inductance L_{m1} is released to the low-voltage side V_L through the body diode D_{S1} of switch S1, and mode 1 ends. The equivalent circuit diagram of mode 1 is shown in Figure 7a.

Mode 2 (t_1–t_2)

The interval begins when $t = t_1$. Switch signals V_{gs1} and V_{gs3} are in the ON state, whereas switch signals V_{gs2} and V_{gs4} are in the OFF state. L_{lk3} is magnetized by C3 through S3; causing current i_{S3} to increase linearly. Part of the energy stored in C3 is transmitted to the magnetizing inductance L_{m1} by the transformer. L_{m1} and capacitor C1 release energy to the low-voltage side V_L and capacitor C2, and mode 2 ends. The equivalent circuit diagram of is shown as Figure 7b.

Mode 3 (t_2–t_3)

At the beginning of this mode, when $t = t_2$, switch signals V_{gs1} and V_{gs3} are in the ON state, whereas switch signals V_{gs2} and V_{gs4} are in the OFF state. Moreover, the current direction of i_{S3} is reversed. The high-voltage side V_H transfers energy to L_{lk3} and C3. Capacitor C2 provides energy to capacitor C1. At the same time, the magnetizing

inductance L_{m1} releases energy to the low-voltage side V_L. When all switch signals are in the OFF state, mode 3 ends. The equivalent circuit diagram is shown in Figure 7c.

Mode 4 (t_3–t_4)

This mode begins when $t = t_3$. All switch signals are in the OFF state. The high-voltage side V_H charges the parasitic capacitance C_{S3} of switch S3 until it is turned OFF, and the leakage inductance L_{lk3} extracts energy from the parasitic capacitance C_{S4} of switch S4 to achieve ZVS. The magnetizing inductance Lm1 begins storing energy and the leakage inductance Llk1 releases energy to the low-voltage side V_L. The leakage inductance L_{lk2} stores energy through the capacitors C2, C1, and the body diode D_{S1} of switch S1, and mode 4 ends. The equivalent circuit diagram is shown in Figure 7d.

Mode 5 (t_4–t_5)

In this mode, switch signals V_{gs1} and V_{gs3} are in the OFF state and switch signals V_{gs2} and V_{gs4} are in the ON state. The leakage inductance L_{lk3} releases energy to capacitor C3 until the current i_{Llk3} is zero. The leakage inductance L_{lk1} releases energy to the magnetizing inductance Lm1. Capacitor C1 releases energy to capacitor C2 and to the low-voltage side V_L, at which point mode 5 ends. The equivalent circuit diagram of mode 5 is shown in Figure 7e.

Mode 6 (t_5–t_6)

This mode begins when $t = t_5$. Switch signals V_{gs1} and V_{gs3} are in the OFF state and switch signals V_{gs2} and V_{gs4} are in the ON state. The leakage inductance L_{lk3} is magnetized through S4; therefore, the current i_{S4} increases linearly. Part of the energy stored in capacitor C3 is transferred to the magnetizing inductance L_{m1} through the transformer. Capacitor C1 continues to supply energy to L_{m1} and to the low-voltage side V_L. When the current of switch S2 drops to zero, mode 6 ends. The equivalent circuit diagram is shown in Figure 7f.

Mode 7 (t_6–t_7)

At the beginning of this mode, when $t = t_6$, switch signals V_{gs1} and V_{gs3} are in the OFF state, whereas switch signals V_{gs2} and V_{gs4} are in the ON state. The transformer continuously transmits the energy of the magnetizing inductance L_{m1} to capacitor C3, which stores it. Capacitor C2 is an energy storage state through switch S2. Capacitor C1 releases energy to the low-voltage side V_L, at which point mode 7 ends. The equivalent circuit diagram is shown in Figure 7g.
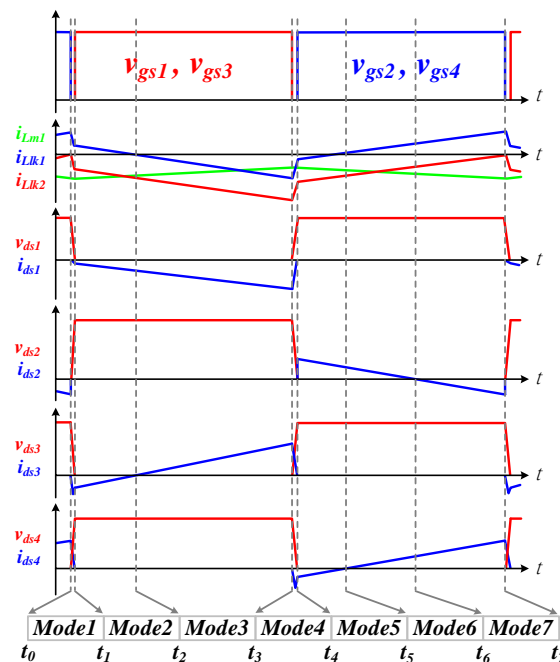

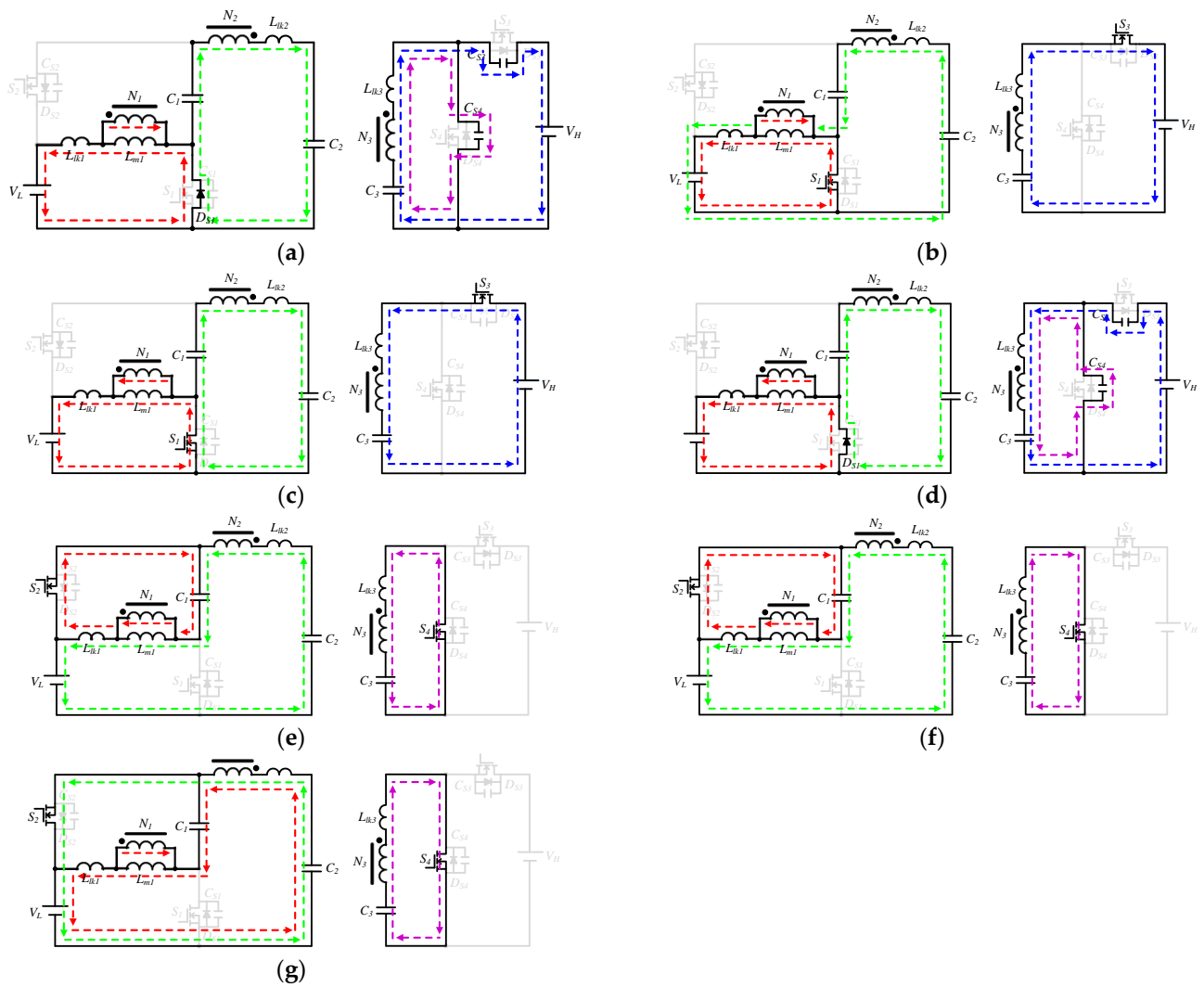**Figure 6.** Key waveforms of the proposed topology in the step-down mode.

Figure 7. Equivalent circuit diagrams of (**a**) mode 1, (**b**) mode 2, (**c**) mode 3, (**d**) mode 4, (**e**) mode 5, (**f**) mode 6, and (**g**) mode 7 in the step-down mode.

3. Steady-State Analysis

Regarding the analysis of the circuit operated in CCM mode, in the step-up mode, the switching period is TS. Switch signal V_{gs1} is turned ON for time D1TS and turned OFF for time $(1 - D1)$TS. In the step-down mode, the switching period is TS, switch signals V_{gs1} and V_{gs3} are turned ON for time D3TS and turned OFF for time $(1 - D3)$TS. The following assumptions must be made:

(1) All components are ideal. The internal resistance and parasitic effects are ignored.
(2) The capacitance of all capacitors is infinite, making the capacitor voltage constant.
(3) The leakage inductance of the transformer is ignored.
(4) The circuit operating modes with short durations are ignored.
(5) For easier calculation, the ideal transformer is represented as $N = N_1/N_3 = N_2/N_3$, where N is the transformer turns ratio.

3.1. Step-Up Mode

3.1.1. Voltage Gain Analysis

Derived from Figure 3, V_H is the sum of the voltage induced by V_L through the turns ratio N and through V_{C3}. It can be expressed as

$$V_H = NV_L + V_{C3} \tag{1}$$

To determine the relationship between V_H and V_L, the relationships of V_{C1}, V_{C2}, and V_{C3} with V_L must be identified.

During $D_1 T_S$, switch signal V_{gs1} is turned ON. According to Kirchhoff's voltage law (KVL), voltage V_{Lm1} can be expressed as

$$V_{Lm1} = V_L = V_{C1} - V_{C2} = L_{m1} \frac{\Delta i_{Lm1,on}}{D_1 T_s} \tag{2}$$

During $(1 - D_1) T_S$, switch signal V_{gs1} is turned *OFF*. According to KVL, voltage V_{Lm1} can be obtained as follows:

$$V_{Lm1} = V_{C1} = \frac{V_{C3}}{N} = L_{m1} \frac{\Delta i_{Lm1,off}}{(1 - D_1) T_S} \tag{3}$$

On the basis of the volt–second balance of inductance, the amount of change in current during a switching period must be zero in the steady state. This premise is expressed as

$$\Delta i_{Lm1,on} = \Delta i_{Lm1,off} \tag{4}$$

Substituting Equations (2) and (3) into Equation (4), voltages V_{C1}, V_{C2}, and V_{C3} can be respectively obtained as follows:

$$V_{C1} = \frac{D_1}{1 - D_1} V_L \tag{5}$$

$$V_{C2} = \frac{2D_1 - 1}{1 - D_1} V_L \tag{6}$$

$$V_{C3} = D_1 V_H \tag{7}$$

Finally, substituting Equation (7) into Equation (1), the voltage gain in step-up mode Gstep-up can be derived as

$$G_{step-up} = \frac{V_H}{V_L} = \frac{N}{1 - D_1} \tag{8}$$

With reference to Equation (8), the relationships among the voltage gain in step-up mode Gstep-up, the duty ratio D_1, and the turns ratio N are visualized (Figure 8).
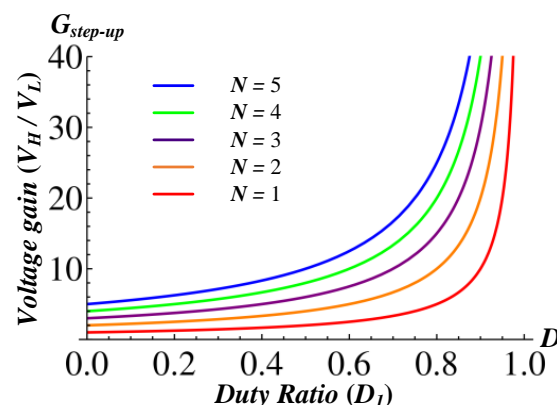

Figure 8. Voltage gain of the proposed topology in the step-up mode.

3.1.2. Voltage Stress Analysis of Components

According to the equivalent circuit diagram for the $D_1 T_S$ period, the voltage across $S1$ is the sum of V_L and V_{C1}, and the voltage stress on $S3$ is V_H. The voltage stress on $S1$ and $S3$ can be respectively expressed as

$$V_{S1,stress} = V_L + V_{C1} = \frac{1}{1 - D_1} V_L = \frac{1}{N} V_H \tag{9}$$

and

$$V_{S3,stress} = V_H = \frac{N}{1 - D_1} V_L \tag{10}$$

On the basis of the equivalent circuit diagram for the $(1 - D_1)T_S$ period, the voltage stress on S2 is the sum of V_L and V_{C1}, and the voltage stress on S4 is V_H. The voltage across S2 and S4 can be respectively determined as

$$V_{S2,stress} = V_L + V_{C1} = \frac{1}{1 - D_1} V_L = \frac{1}{N} V_H \tag{11}$$

and

$$V_{S4,stress} = V_H = \frac{N}{1 - D_1} V_L \tag{12}$$

3.1.3. Design of the Magnetic Components

The magnetic components of the proposed topology are designed in *CCM* mode. The maximum current of L_{m1} can be expressed as

$$i_{Lm1,max} = i_{Lm1,avg} + \frac{\Delta i_{Lm1}}{2} \tag{13}$$

and the minimum current of L_{m1} is given by

$$i_{Lm1,min} = i_{Lm1,avg} - \frac{\Delta i_{Lm1}}{2} \tag{14}$$

The current Δi_{Lm1} and $i_{Lm1,avg}$ can be respectively determined as

$$\Delta i_{Lm1} = \frac{V_{Lm1}}{L_{m1}} D_1 T_S = \frac{(1 - D_1)D_1}{L_{m1} f_s N} V_H \tag{15}$$

and

$$i_{Lm1,avg} = i_L = \frac{N}{1 - D_1} i_H \tag{16}$$

Because the magnetic components are designed in *CCM* mode, current $i_{Lm1,min}$ must be greater than zero. When the magnetic components are operated in boundary conduction mode (*BCM*), current $i_{Lm1,min}$ is equal to zero. Substituting Equations (15) and (16) into Equation (14), current $i_{Lm1,min}$ can be expressed as

$$i_{Lm1,min} = 0 = \frac{N}{1 - D_1} i_H - \frac{(1 - D_1)D_1}{2L_{m1} f_s N} V_H \tag{17}$$

On the basis of Equation (17), the formula for the operation of L_{m1} in *BCM* mode is expressed as

$$L_{m1,BCM} = \frac{(1 - D_1)^2 D_1}{2 f_s N^2} \frac{V_H}{i_{H,BCM}} \tag{18}$$

The design parameters of the magnetic components in the step-up mode are presented as follows. The turns ratio N is 5, the switching frequency fs is 50 kHz, the voltage of the high-voltage side V_H is 400 V, and the current of the high-voltage side i_H is 0.375 A.

Substituting these parameters into Equation (18), the curve of L_{m1} operated in *BCM* mode is plotted (Figure 9). When the value of L_{m1} is greater than the curve in *BCM* mode, L_{m1} is operated in *CCM* mode; otherwise, L_{m1} is operated in *DCM* mode.
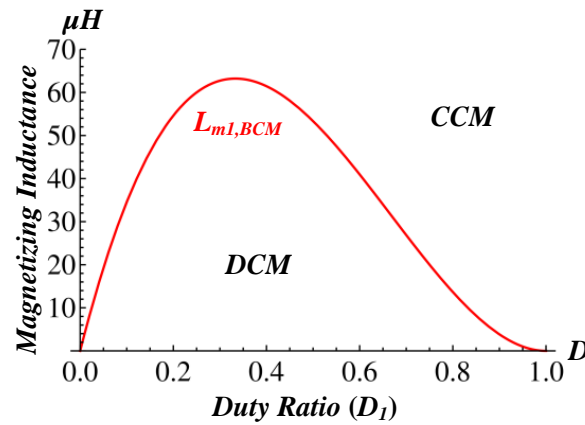
Figure 9. Curve of $L_{m1,BCM}$ in the step-up mode.

3.2. Step-Down Mode

3.2.1. Voltage Gain Analysis

To derive the relationship between V_L and V_H, the respective relationships of V_{C1}, V_{C2}, and V_{C3} with V_L must also be derived.

Switch signals V_{gs1} and V_{gs3} are turned ON during $D_3 T_S$. According to KVL, voltage V_{Lm1} can be expressed as

$$V_{Lm1} = V_L = V_{C1} - V_{C2} = L_{m1} \frac{\Delta i_{Lm1,on}}{D_3 T_S} \tag{19}$$

During $(1 - D_3)T_S$, switch signal V_{gs3} is turned *OFF*. According to KVL, the voltage V_{Lm1} can be obtained as

$$V_{Lm1} = \frac{V_{C3}}{N} = L_{m1} \frac{\Delta i_{m1,off}}{(1 - D_6)T_S} \tag{20}$$

According to the volt–second balance of inductance, the amount of change in the current during a switching period must be zero in the steady state. This premise is expressed as

$$\Delta i_{Lm1,on} = \Delta i_{Lm1,off} \tag{21}$$

Substituting Equations (19) and (20) into Equation (21), the voltages of C1, C2, and C3 can be respectively obtained:

$$V_{C1} = \frac{D_3}{1 - D_3} V_L \tag{22}$$

$$V_{C2} = \frac{2D_3 - 1}{1 - D_1} V_L \tag{23}$$

$$V_{C3} = D_3 V_H \tag{24}$$

Finally, substituting Equation (24) into Equation (1), the voltage gain in the step-up mode Gstep-down can be derived as

$$G_{step-down} = \frac{V_H}{V_L} = \frac{1 - D_3}{N} \tag{25}$$

On the basis of Equation (25), the relationships among the voltage gain in the step-down mode Gstep-down, the duty ratio D_3, and the turns ratio N are visualized (Figure 10).
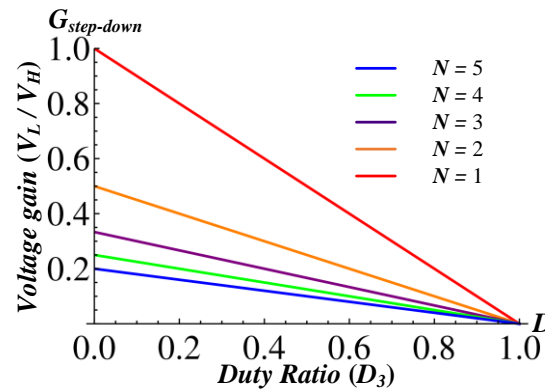
Figure 10. Voltage gain of the proposed topology in the step-down mode.

3.2.2. Voltage Stress Analysis of Components

On the basis of the equivalent circuit during D_3T_S, the voltage stress on $S1$ is the sum of V_L and V_{C1}, and the voltage across $S3$ is V_H. The voltage across $S1$ and $S3$ can be respectively obtained as

$$V_{S1,stress} = V_L + V_{C1} = \frac{1}{1 - D_3}V_L = \frac{1}{N}V_H \qquad (26)$$

and

$$V_{S3,stress} = V_H = \frac{N}{1 - D_3}V_L \qquad (27)$$

According to the equivalent circuit diagram for the $(1 - D_3)T_S$ period, the voltage across $S2$ is the sum of V_L and V_{C1}, and the voltage across $S4$ is V_H. The voltages across $S2$, and $S4$ can be expressed as

$$V_{S2,stress} = V_L + V_{C1} = \frac{1}{1 - D_3}V_L = \frac{1}{N}V_H \qquad (28)$$

and

$$V_{S4,stress} = V_H = \frac{N}{1 - D_3}V_L \qquad (29)$$

3.2.3. Design of the Magnetic Components

The maximum current of L_{m1} is given by

$$i_{Lm1,max} = i_{Lm1,avg} + \frac{\Delta i_{Lm1}}{2} \qquad (30)$$

and the minimum current of L_{m1} is given by

$$i_{Lm1,min} = i_{Lm1,avg} - \frac{\Delta i_{Lm1}}{2} \qquad (31)$$

Currents Δi_{Lm1} and $i_{Lm1,avg}$ can be determined as

$$\Delta i_{Lm1} = \frac{V_{Lm1}}{L_{m1}}D_3T_S = \frac{D_3}{L_{m1}f_s}V_L \qquad (32)$$

and

$$i_{Lm1,avg} = i_L \qquad (33)$$

When the magnetic components are operated in *BCM* mode, current $i_{Lm1,min}$ is equal to zero. Substituting Equations (32) and (33) into Equation (31), current $i_{L1,min}$ can be obtained as

$$i_{Lm1,min} = 0 = i_L - \frac{D_3}{L_{m1}f_s} V_L \qquad (34)$$

As

$$i_{Lm1,BCM} = \frac{D_3}{f_s} \frac{V_L}{i_{L,BCM}} \qquad (35)$$

The design parameters of the magnetic components in the step-up mode are presented as follows. The switching frequency f_s is 50 kHz, the low-voltage side V_L is 36 V, and the current of the low-voltage side i_L is 4.167 A.

Substituting the parameters into Equation (35), the curve of L_{m1} operated in *BCM* mode is plotted (Figure 11). When the value of L_{m1} is greater than the curve in BCM mode, L_{m1} is operated in *CCM* mode; otherwise, it is operated in *DCM* mode.
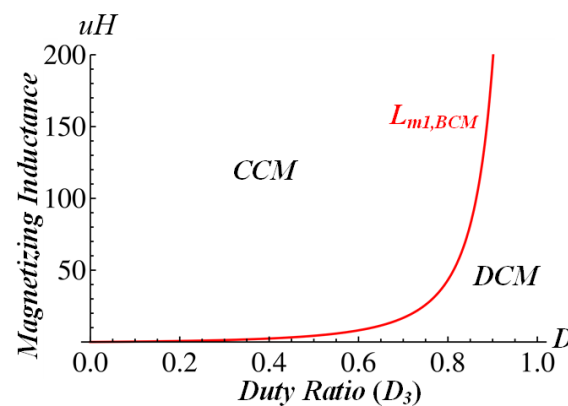

Figure 11. Curve of $L_{m1,BCM}$ in step-down mode.

4. Experimental Results

Key waveforms in the step-up and step-down modes were measured. The prototype of the proposed bidirectional isolated DC–DC converter is shown in Figure 12. The electrical specifications and component parameters are listed in Table 1, and the voltage stress on each component is considered. Figure 13 shows the control scheme, dsPIC30F4011 is used to generate the PWM signals to control the converter by gate driver circuit. To verify the feasibility of the proposed topology, the measured waveforms are examined.
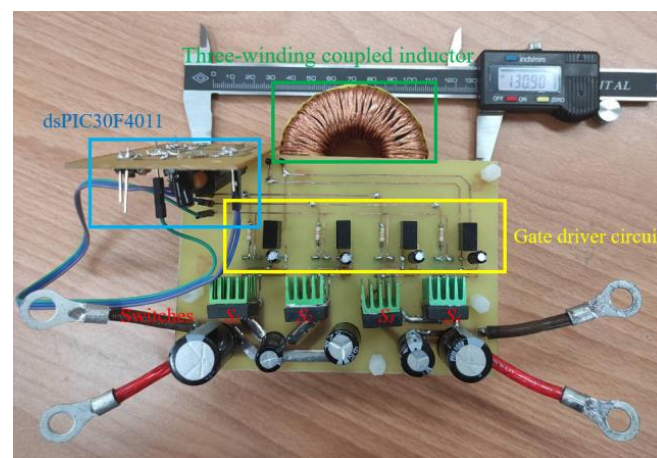

Figure 12. Photograph of the proposed topology.

Table 1. Electrical specifications and component parameters of the proposed converter.

| Parameter	Specification	Parameter	Specification
High-side voltage V_H	400 V	Switching frequency fs	50 kHz
Low-side voltage V_L	36 V	Magnetizing inductance L_{m1}	47 µH
High-side power P_H	500 W	Leakage inductance L_{lk1}	4 µH
Low-side power P_L	500 W	Leakage inductance L_{lk2}	4 µH
Power switches S_1 and S_2	IRFP4568PbF	Capacitor C_1	100 µF
Power switches S_3 and S_4	IXFH26N50Q	Capacitor C_2	100 µF
Turns ration N	5	Capacitor C_3	100 µF
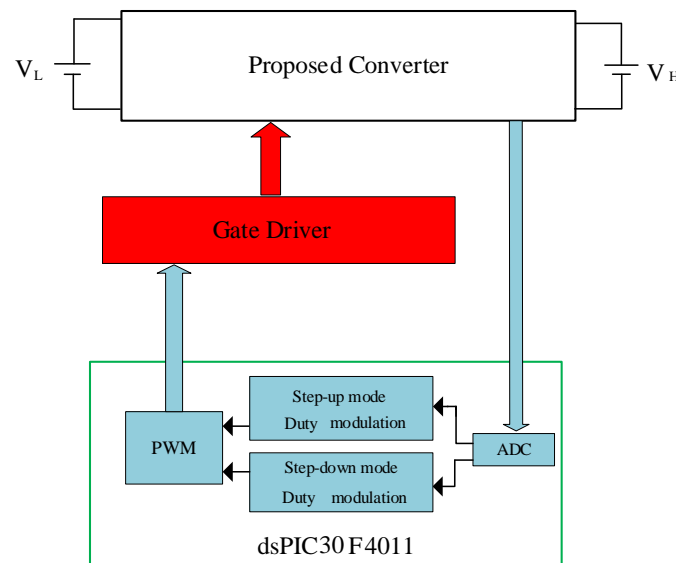
Figure 13. The control scheme of the proposed converter.

Figure 14 presents the measured waveforms in the step-up mode under the full 500 W load. As shown in Figure 14a–c, respectively, Dstep−up is approximately 0.6, the voltage stress of switches S1 and S2 is 80 V, and the voltage stress of switches S3 and S4 is 400 V. Moreover, switches S1 and S2 have the ZVS feature in the step-up mode. In Figure 14d, the voltage stress of C1, C2, and C3 is 54, 18, and 240 V, respectively.

The waveforms measured in the step-down mode under the full load are displayed in Figure 15. As presented in Figure 15a–c, Dstep−down is approximately 0.6, the voltage stress of switches S1 and S2 is 80 V, and the voltage stress of switches S3 and S4 is 400 V. In this mode, switches S3 and S4 clearly have the ZVS feature, and switches S1 and S2 possess the synchronous rectification function. In Figure 15d, the voltage stress of C1, C2, and C3 is 54, 18, and 240 V, respectively.

Figure 16a,b shows the measured waveforms of the proposed topology operated under load variation in step-up mode and step-down mode, respectively, while the output load is step changed between half load and full load. It can be seen that the output voltage (V_H/V_L) is very stable and is not greatly affected by load changes.

Figure 17 shows the energy conversion efficiency of the proposed topology in the step-up mode. The highest energy conversion efficiency is 95.74% at 150 W, and the lowest is 92.76% at 500 W. The curve of the energy conversion efficiency of the proposed topology in step-down mode is plotted in Figure 18. The highest energy conversion efficiency is 96.13% at 200 W, and the lowest is 93.67% at 500 W.
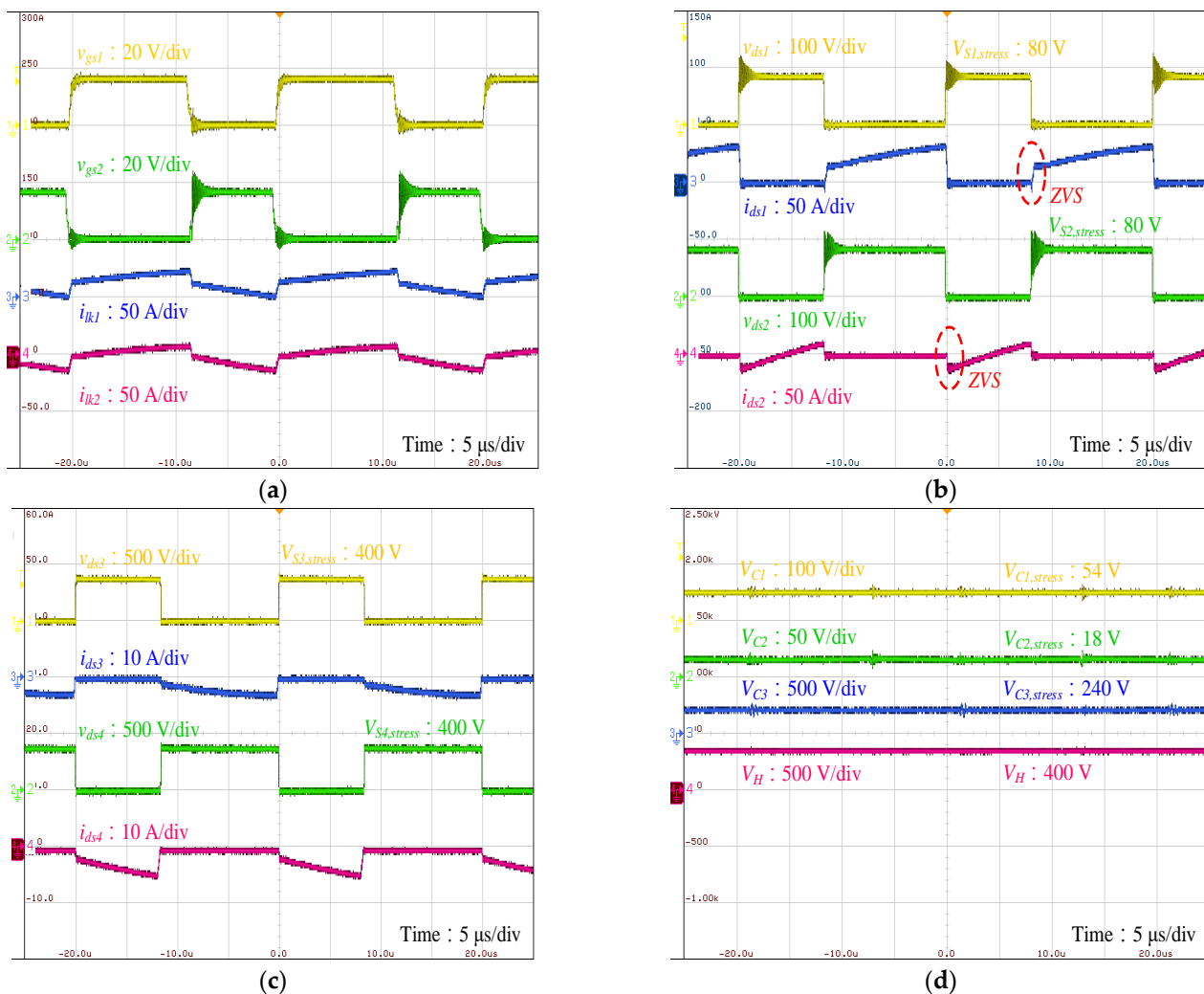
Figure 14. Experimental results of the proposed topology, operated in the step-up mode under the full load (500 W): (**a**) V_{gs1}, V_{gs2}, i_{lk1}, and i_{lk2}; (**b**) V_{ds} and i_{ds} of S1 and S2; (**c**) V_{ds} and i_{ds} of S3 and S4; and (**d**) V_{C1}, V_{C2}, V_{C3}, and V_H.

The performance of the proposed converter is examined, and its advantages and disadvantages are determined. Table 2 presents a comparison of the proposed converter with other bidirectional converters in [26,28,30] in terms of component numbers, ripple currents, electrical specifications, and other parameters.

Figures 19 and 20 compare the voltage gain of the proposed converter in the step-up and step-down mode, respectively, with those of the bidirectional converters in [26,28,30]. Although the converter in [26] has a higher voltage gain than the proposed converter in the step-up mode, it has neither a common ground nor an isolated ground. The voltage gains of the converters in [28,30] are lower than that of the proposed converter. Moreover, given that the proposed converter has a duty ratio Dstep−down of approximately 0.6, its voltage gain exceeds those of the converters in [26,28,30] in the step-down mode.

Figure 21 compares the energy conversion efficiency of the proposed converter in step-up mode with those of the converters in [26,28,30]. Although the energy conversion efficiency of the converter in [26] in the step-up mode exceeds that of the proposed converter, as mentioned, it has neither a common ground nor an isolated ground between the low- and high-voltage sides, reducing its safety and industrial applicability. Overall, the energy conversion efficiency and cost of the proposed converter are superior to those of the converters in [28,30], and its power is superior to those of the converters in [26,28,30].
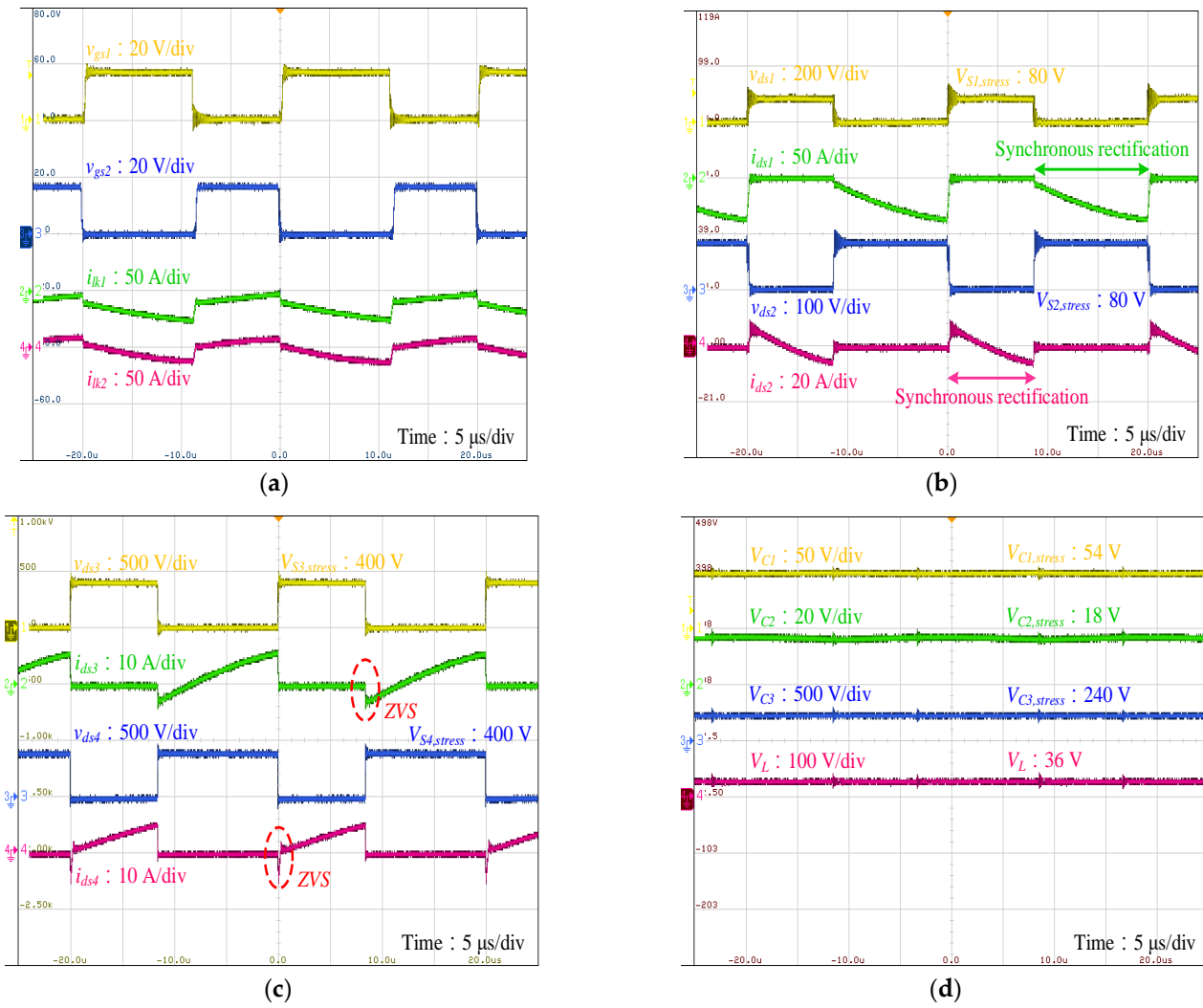
Figure 15. Experimental results of the proposed topology, operated in the step-down mode under the full load (500 W): (**a**) V_{gs1}, V_{gs2}, i_{lk1}, and i_{lk2}; (**b**) V_{ds} and i_{ds} of S1 and S2; (**c**) V_{ds} and i_{ds} of S3 and S4; and (**d**) V_{C1}, V_{C2}, V_{C3}, and V_L.
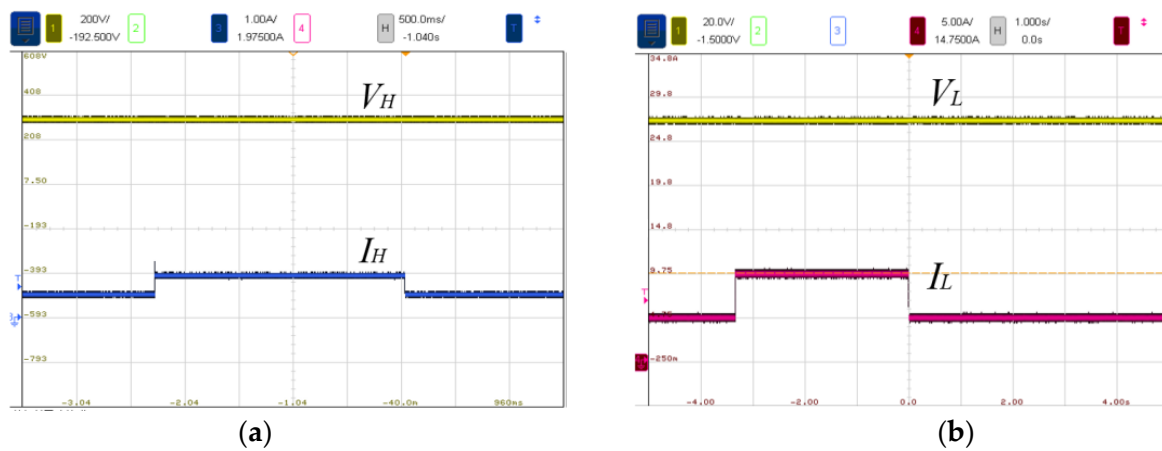

Figure 16. Measured waveforms of load variation of the proposed topology: (**a**) step-up mode, and (**b**) step-down mode.
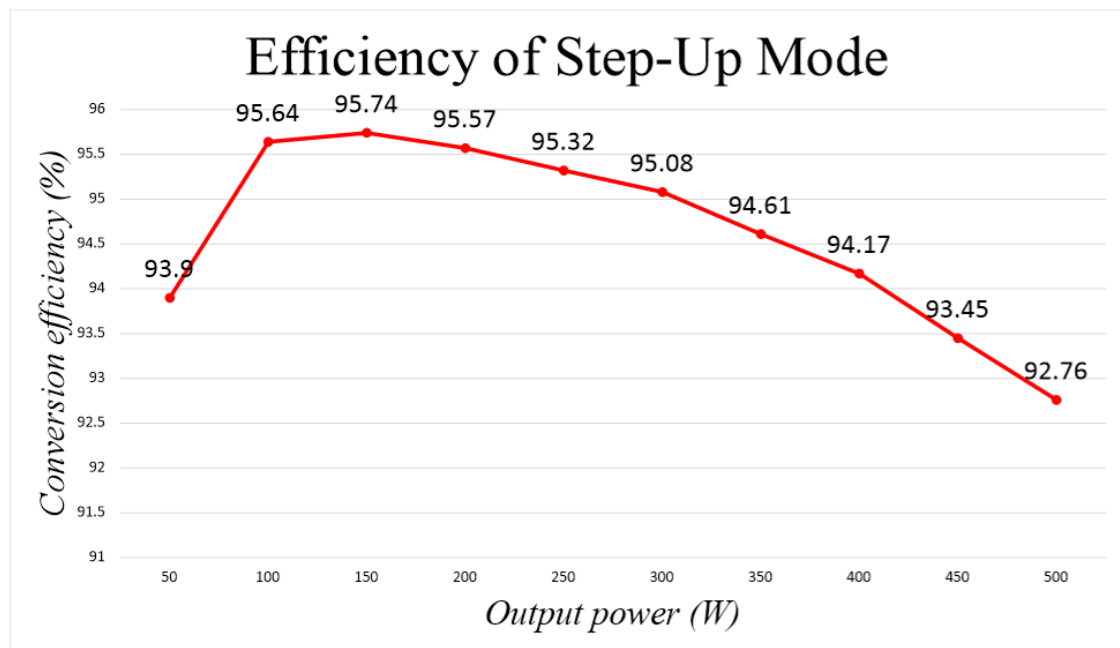
Figure 17. Energy conversion efficiency curve of the proposed topology in the step-up mode.
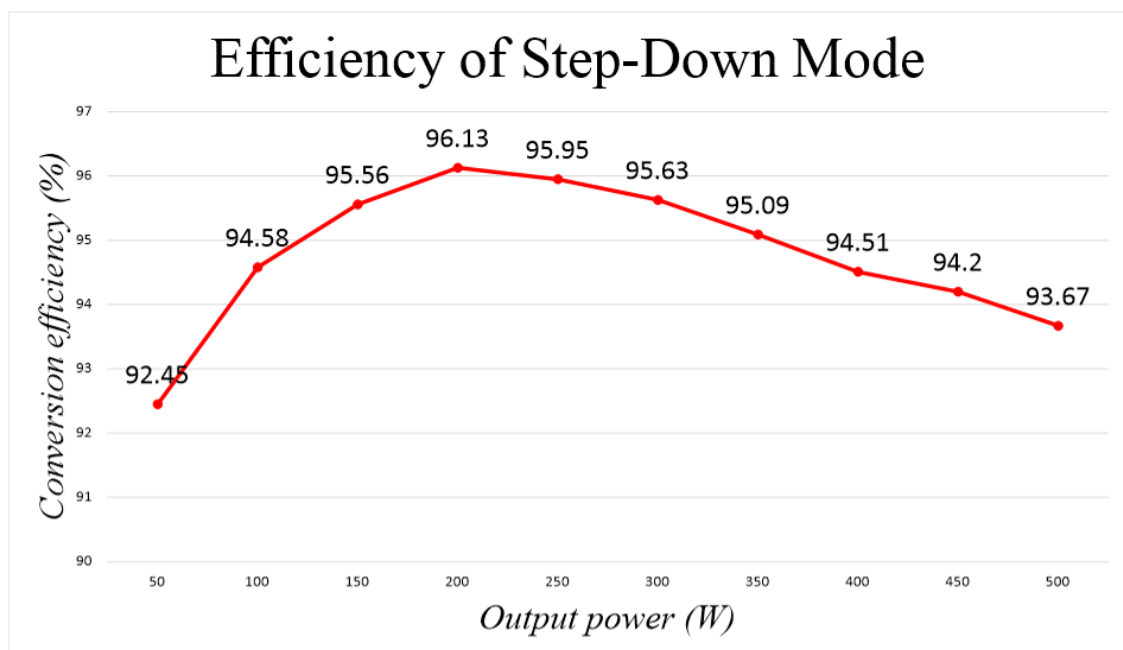

Figure 18. Energy conversion efficiency of the proposed topology in the step-down mode.
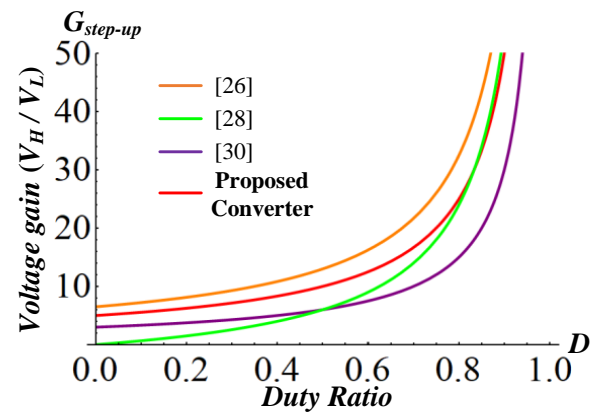
Figure 19. Comparison of voltage gains in step-up mode of the proposed converter and other bidirectional converters (in [26,28,30]).

Table 2. Comparison of the proposed bidirectional converter with other studies.

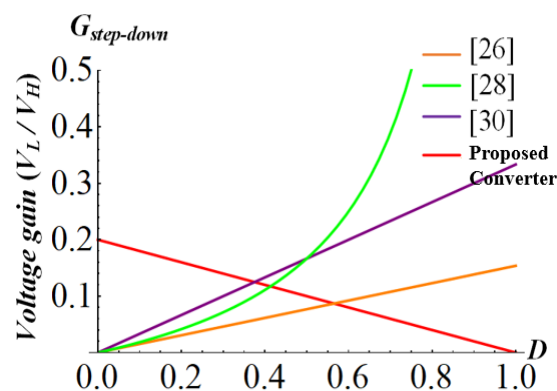|	Converter in [26]	Converter in [28]	Converter in [30]	Proposed Converter
$G_{step-up}\left(\frac{V_H}{V_L}\right)$	$\frac{2+N}{1-D}$	$\frac{2N}{1-D}$	$\frac{2ND}{1-D}$	$\frac{N}{1-D}$
$G_{step-down}\left(\frac{V_L}{V_H}\right)$	$\frac{D}{2+N}$	$\frac{D}{2N}$	$\frac{D}{2N(1-D)}$	$\frac{1-D}{N}$
MOSFETs	4	4	4	4
Inductors	0	2	1	0
Transformers	1	1	2	1
Capacitors	2	1	4	3
Diodes	0	0	6	0
Turns ratio	1:4.5	1:1.5	1:3	1:5
The current ripple of low voltage side	Normal	Normal	Large	Normal
Low side Voltage V_L	30 V	24 V	48 V	36 V
High side Voltage V_H	380 V	200 V	400 V	400 V
Switching frequency f_S	50 kHz	50 kHz	40 kHz	50 kHz
Output power	300 W	200 W	400 W	500 W
Isolated	No	Yes	Yes	Yes

Figure 20. Comparison of voltage gains in step-down mode of the proposed converter and the converters in [26,28,30].
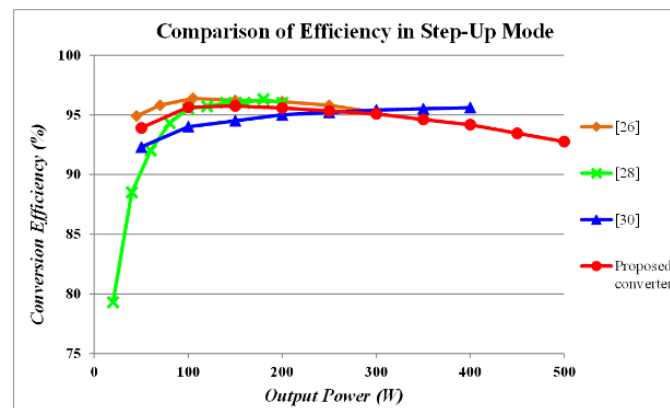
Figure 21. Comparison of the energy conversion efficiency of the proposed converter in the step-up mode with those of the converters in [26,28,30].

Figure 22 compares the energy conversion efficiency of the proposed converter in step-down mode with those of the converters in [26,28,30]. The energy conversion efficiencies of the converter in [26] operating under a light load and of the converter in [30] operating under the full load exceed that of the proposed converter. In addition, the conversion efficiencies of the proposed converter surpass those of the converters in [26,28,30]. Furthermore, the magnetic flux of the converter in [28] is unbalanced on the low-voltage side, and the excessive number of magnetic components increases the circuit volume and cost and leads to the high loss of copper wire. Although the converter in [30] has an energy recovery feature, the conduction loss on the components is relatively high.
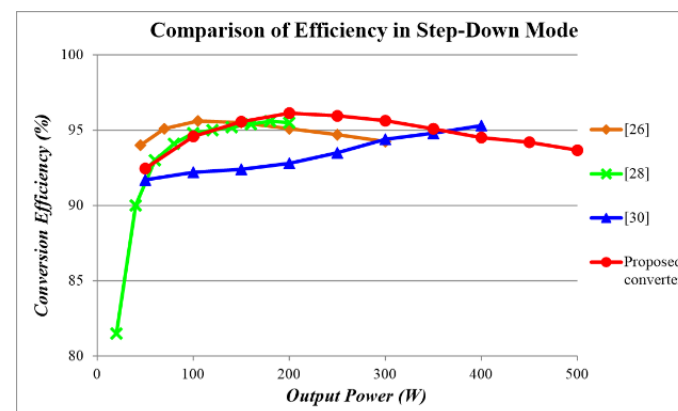

Figure 22. Comparison of the energy conversion efficiency of the proposed converter in the step-down mode with those of the converters in [26,28,30].

5. Discussion and Conclusions

This paper presents a novel isolated bidirectional DC–DC converter for application in PHEVs. The proposed converter consists of a three-winding coupled inductor, three switched capacitors, and four active switches. Energy from the leakage inductance can be effectively recycled in both the step-up and step-down modes, and all switches have the ZVS feature. The advantages of the proposed topology are as follows: (1) it has high energy conversion efficiency, (2) it is safe to use and has relatively low circuit costs, (3) all power switches can achieve ZVS, (4) an inductance circuit is employed to facilitate energy recovery, and (5) the low-voltage side has the synchronous rectification function in step-down mode. However, the limitations of the proposed converter in this paper include: (1) the implemented power is too low to be truly applied to the EV system; (2) the input voltage range is too narrow, which limits the application of the converter; (3) it is not actually considered the charging method of the battery, which will affect the life of the battery; and (4) only the dual-port power transmission direction, which will limit the

application of the converter. Therefore, the future research direction of this work is to improve the above restrictions.

References

1. Drees, T.; Bracht, N.V.; Moser, A. Reserve providing in future generation systems considering renewable energy sources. In Proceedings of the 11th International Conference on the European Energy Market (EEM14), Krakow, Poland, 28–30 May 2014; Volume 14, pp. 1–6.

2. Ahmed, A.; Jiang, T. Operation Management of Power Grid System with Renewable Energy Sources and Energy Storage System Integrations. In Proceedings of the 2nd IEEE Conference on Energy Internet and Energy System Integration, Beijing, China, 20–22 October 2018; pp. 1–6.

3. Dahale, S.; Das, A.; Pindoriya, N.M.; Rajendran, S. An overview of DC-DC converter topologies and controls in DC microgrid. In Proceedings of the 7th International Conference on Power Systems (ICPS), Pune, India, 21–23 December 2017; pp. 410–415.

4. Lonkar, M.; Ponnaluri, S. An overview of DC microgrid operation and control. In Proceedings of the IREC2015 the Sixth International Renewable Energy Congress, Sousse, Tunisia, 24–26 March 2015; pp. 1–6. [CrossRef]

5. Joshi, R.P.; Deshmukh, A.P. Hybrid Electric Vehicles: The Next Generation Automobile Revolution. In Proceedings of the IEEE Conference on Electric and Hybrid Vehicles, Pune, India, 18–20 December 2006; pp. 1–6.

6. Song, E.; Yao, C.; Fan, L. Analysis and investigation on PHEV Economy flow. In Proceedings of the 2011 International Conference on Electronics, Communications and Control (ICECC), Ningbo, China, 9–11 September 2011; pp. 4172–4175.

7. Klassen, S.V.; Klassen, T.S.; Shtein, D.; Volkov, A.G.; Dubkova, R.Y.; Luft, S. Study of a Dual-Loop Subordinate Control System for a DC-DC Converter with Galvanic Isolation. In Proceedings of the 19th International Conference of Young Specialists on Micro/Nanotechnologies and Electron Devices, Erlagol, Russia, 29 June–3 July 2018; pp. 6403–6410.

8. Hsieh, Y.-C.; Chang, Y.-N.; Lee, K.-Y.; Chiu, Y.-C.; Wu, W.-T. Bidirectional softly switched dc-to-dc converter with galvanic isolation. In Proceedings of the 2015 IEEE International Conference on Industrial Technology (ICIT), Seville, Spain, 17–19 March 2015; pp. 952–956.

9. Arnaudov, D.; Hinov, N.; Vuchev, S.; Nedyalkov, I. Converter with galvanic isolation for supercapacitor charging. In Proceedings of the 19th International Symposium on Electrical Apparatus and Technologies (SIELA), Bourgas, Bulgaria, 29 May–1 June 2016; pp. 1–4.

10. Hu, J.; Xiao, W.; Zhang, B.; Qiu, D.; Ho, C.N.M. A Single Phase Hybrid Interleaved Parallel Boost PFC Converter. In Proceedings of the Energy Conversion Congress and Exposition (ECCE), Portland, OR, USA, 23–27 September 2018; pp. 2855–2859.

11. Ancuti, M.-C.; Svoboda, M.; Musuroi, S.; Hedes, A.; Olarescu, N.-V. Boost PFC converter versus bridgeless boost PFC converter EMI analysis. In Proceedings of the 2014 International Conference on Applied and Theoretical Electricity (ICATE), Craiova, Romania, 23–25 October 2014; pp. 1–6.

12. Ye, Z.; Sun, B. PFC efficency improvement and THD reduction at light loads with ZVS and valley switching. In Proceedings of the Twenty-Seventh Annual IEEE Applied Power Electronics Conference and Exposition (APEC), Coronado Springs, OR, USA, 5–9 February 2012; pp. 802–806.

13. Harrag, A.; Messalti, S.; Daili, Y. Innovative Single Sensor Neural Network PV MPPT. In Proceedings of the 2019 6th International Conference on Control, Decision and Information Technologies (CoDIT), Paris, France, 26–29 April 2019; pp. 1895–1899.

14. Messalti, S.; Harrag, A.G.; Loukriz, A.E. A new neural networks MPPT controller for PV systems. In Proceedings of the IREC2015 The Sixth International Renewable Energy Congress, Sousse, Tunisia, 24–26 March 2015; pp. 1–6.

15. Singh, A.; Shimi, S.L. MATLAB / SIMULINK Simulation of PV System Based on MPPT in Variable Irradiance with EV Battery as Load. In Proceedings of the International Conference on Computational Intelligence and Computing Research (ICCIC), Timilnadu, India, 14–16 December 2017; pp. 1–4.

16. Tintu, V.R.; George, M. Tapped inductor technology based DC-DC converter. In Proceedings of the 2011 International Conference on Signal Processing, Communication, Computing and Networking Technologies, Thuckalay, India, 21–22 July 2011; pp. 747–753.

17. Yris, J.C.; Calleja, J.H.; González, L.H.; López, L.M.; Martínez, R.P. Analysis of tapped inductor converters in three operating modes for photovoltaic systems with grounded source. In Proceedings of the 12th IEEE International Power Electronics Congress, San Luis Potosi, Mexico, 22–25 August 2010; pp. 215–220.

18. Vazquez, N.; Estrada, L.; Hernandez, C.; Rodriguez, E. The Tapped-Inductor Boost Converter. In Proceedings of the International Symposium on Industrial Electronics, Vigo, Spain, 4–7 June 2007; pp. 538–543.

19. Mohammed, A.A.; Nafie, S.M. Flyback converter design for low power application. In Proceedings of the 2015 International Conference on Computing, Control, Networking, Electronics and Embedded Systems Engineering (ICCNEEE), Khartoum, Sudan, 7–9 September 2015; pp. 447–450.

20. Hsieh, Y.; Chen, J.; Yang, L.; Wu, C.; Liu, W. High-Conversion-Ratio Bidirectional DC–DC Converter with Coupled In-ductor. *IEEE Trans. Ind. Electron.* **2014**, *61*, 210–222. [CrossRef]

21. Aamir, M.; Mekhilef, S.; Kim, H.-J. High-Gain Zero-Voltage Switching Bidirectional Converter with a Reduced Number of Switches. *IEEE Trans. Circuits Syst. II Express Briefs* **2015**, *62*, 816–820. [CrossRef]

22. Dung, N.A.; Chiu, H.-J.; Liu, Y.-C.; Huang, P.J. Analysis and Implementation of a High Voltage Gain 1 MHz Bidirectional DC–DC Converter. *Trans. Ind. Electron.* **2020**, *67*, 1415–1424. [CrossRef]

23. Omara, A.M.; Sleptsov, M. Bidirectional interleaved DC/DC converter for electric vehicle application. In Proceedings of the 11th International Forum on Strategic Technology (IFOST), Novosibirsk, Russia, 1–3 June 2016; pp. 100–104.

24. Bahrami, H.; Farhangi, S.; Iman-Eini, H.; Adib, E. A New Interleaved Coupled-Inductor Nonisolated Soft-Switching Bidirectional DC–DC Converter with High Voltage Gain Ratio. *IEEE Trans. Ind. Electron.* **2017**, *65*, 5529–5538. [CrossRef]

25. Yang, Y.; Ma, J.; Ho, C.N.-M.; Zou, Y. A New Coupled-Inductor Structure for Interleaving Bidirectional DC-DC Converters. *IEEE J. Emerg. Sel. Top. Power Electron.* **2015**, *3*, 841–849. [CrossRef]

26. Hassan, W.; Soon, J.L.; Lu, D.D.-C.; Xiao, W. A High Conversion Ratio and High-Efficiency Bidirectional DC–DC Converter with Reduced Voltage Stress. *IEEE Trans. Power Electron.* **2020**, *35*, 11827–11842. [CrossRef]

27. Hosseinzadeh, Z.; Molavi, N.; Farzanehfard, H. Soft-Switching High Step-Up/Down Bidirectional DC–DC Converter. *IEEE Trans. Ind. Electron.* **2019**, *66*, 4379–4386. [CrossRef]

28. Liang, T.-J.; Lee, J.-H. Novel High-Conversion-Ratio High-Efficiency Isolated Bidirectional DC–DC Converter. *IEEE Trans. Ind. Electron.* **2014**, *62*, 4492–4503. [CrossRef]

29. Shen, C.; Shen, Y.; Chiu, P.; Liang, T. Isolated bidirectional converter with minimum active switches for high-voltage ratio achievement and micro-grid applications. *IET Power Electron.* **2017**, *10*, 2208–2216. [CrossRef]

30. Shen, C.-L.; Liou, H.; Liang, T.-C.; Gong, H.-Z. An Isolated Bidirectional Interleaved Converter with Minimum Active Switches and High Conversion Ratio. *IEEE Trans. Ind. Electron.* **2017**, *65*, 2313–2321. [CrossRef]

31. Mukhtar, N.M.; Lu, D.D.-C. A Bidirectional Two-Switch Flyback Converter with Cross-Coupled LCD Snubbers for Minimizing Circulating Current. *IEEE Trans. Ind. Electron.* **2019**, *66*, 5948–5957. [CrossRef]

32. Dutta, S.; Maiti, D.; Sil, A.K.; Biswas, S.K. A Soft-Switched Flyback converter with recovery of stored energy in leakage inductance. In Proceedings of the 5th India International Conference on Power Electronics, Delhi, India, 6–8 December 2012; pp. 1–5.

33. Cheng, H.-L.; Chang, Y.-N.; Yen, H.-C.; Hua, C.-C.; Su, P.-S. An Interleaved Flyback-Typed LED Driver with ZVS and Energy Recovery of Leakage Inductance. *IEEE Trans. Power Electron.* **2019**, *34*, 4497–4508. [CrossRef]

34. Lodh, T.; Majumder, T. High gain and efficient integrated flyback-Sepic DC-DC converter with leakage energy recovery mechanism. In Proceedings of the International Conference on Signal Processing, Communication, Power and Embedded System (SCOPES), Paralakhemundi, India, 3–5 October 2016; pp. 1495–1500.

35. Chen, B.; Wang, P.; Wang, Y.-F.; Zhang, S.-H.; Yang, L.; Ji, R.-L. A Bidirectional CDT-LC Resonant DC–DC Converter with a Wide Voltage Range. *IEEE Trans. Ind. Electron.* **2019**, *67*, 2009–2020. [CrossRef]

36. Tseng, K.-C.; Chang, S.-Y.; Cheng, C.-A. Novel Isolated Bidirectional Interleaved Converter for Renewable Energy Applications. *IEEE Trans. Ind. Electron.* **2019**, *66*, 9278–9287. [CrossRef]

37. Lu, J.; Wang, Y.; Li, X. Isolated Bidirectional DC–DC Converter with Quasi-Resonant Zero-Voltage Switching for Battery Charge Equalization. *IEEE Trans. Power Electron.* **2019**, *34*, 4388–4406. [CrossRef]

38. Sha, D.; Chen, D.; Zhang, J. A Bidirectional Three-Level DC–DC Converter with Reduced Circulating Loss and Fully ZVS Achievement for Battery Charging/Discharging. *IEEE J. Emerg. Sel. Top. Power Electron.* **2018**, *6*, 993–1003. [CrossRef]

39. Saadatizadeh, Z.; Babaei, E.; Blaabjerg, F.; Cecati, C. Three-Port High Step-Up and High Step-Down DC-DC Converter with Zero Input Current Ripple. *IEEE Trans. Power Electron.* **2020**, *36*, 1804–1813. [CrossRef]

40. Cheraghi, R.; Adib, E.; Golsorkhi, M.S. A Nonisolated High Step-Up Three-Port Soft-Switched Converter with Minimum witches. *IEEE Trans. Ind. Electron.* **2021**, *68*, 9358–9365. [CrossRef]

41. Faraji, R.; Farzanehfard, H.; Esteki, M.; Khajehoddin, S.A. A Lossless Passive Snubber Circuit for Three-Port DC-DC Converter. *IEEE J. Emerg. Sel. Top. Power Electron.* **2021**, *9*, 1905–1914. [CrossRef]